Broadband Vertical Interconnects Using Slot-Coupled Shielded Microstrip Lines

Norman L. VandenBerg *Member, IEEE,* and Linda P. B. Katehi, *Senior Member, IEEE*

Abstract—**A full-wave space-domain integral equation analysis of aperture coupled shielded microstrip lines is presented based on the Equivalence Principle. The formulation includes the capability to model multi-layered substrates through the derivation of the associated dyadic Green's functions which represent the layers through impedance boundary conditions. The method of moments is used to solve for the line currents and slot voltage with even and odd mode excitations which are then interpreted through transmission line analysis to determine the two-port scattering parameters. A parametric study together with experimental data is presented which demonstrates the behavior of the coupler and the accuracy of the technique.**

I. Introduction

TRANSITIONS from microstrip to slotline have long been recognized as important circuit elements. Two such transitions can be combined to form interconnects between lines and by using lines on opposite sides of the slot plane, a vertical transition is made. The basic structure, in a variety of forms, has a wide range of applications to both broadband and narrowband connections and can be used as a building block for interconnects [1], phase shifters and inverters [2], directional couplers [3], filters [4], and many other microwave components [5].

The advent of monolithic techniques for microwave and millimeter-wave circuits has amplified the need for accurate analysis techniques to account for the effects of shielding structures as well as the interaction between circuit elements which may be closely spaced. These effects may not be accounted for by some methods such as simple transmission line analysis, especially as frequency increases. Additionally, high-frequency interconnect approaches are required which must be accurately modeled for design and also must fit well in a monolithic fabrication scheme. In this regard, the presented approach has significant appeal over via holes since it implements a vertical interconnect while requiring only planar elements which can be accurately modeled.

Numerous investigators have presented approximate analytical techniques to characterize these structures with applications to circuit elements [4]–[8]. A full-wave analysis for microstrip-to-slotline has been reported in [9] with applications to open structures. A quasi-static analysis has been provided in [10], however, this may not be sufficient, particularly for higher frequencies where end effects and higher order mode coupling become more significant. A more recent paper [11] presents a transmission line analysis with excellent results, however, the method does not account for radiation if the structure is open, interactions with the shielding if it is closed as in our case, or other electromagnetic effects which become more severe as frequency is increased. Hybrid methods which combine two-dimensional full-wave analysis with transmission line theory, as in [12], should certainly extend the validity of such models, however, may still not account for all discontinuity effects, especially since it is usually desirable to minimize the overall size which will tend to allow transitions to interact. Our approach uses a three-dimensional full-wave space-domain integral equation method employing the method of moments with Galerkin's procedure to account for all possible interactions.

Manuscript received March 1, 1991; revised July 10, 1991. This work was supported by Texas Instruments under contract UM/EECS:390442, the National Science Foundation under contract ECS:8657951, and by the NASA Center for Space Terahertz Technology.

The authors are with the Radiation Laboratory, the University of Michigan, 1301 Beal Avenue, Ann Arbor, MI 48109-2122.

IEEE Log Number 9103898.

II. Integral Equation Formulation and Network Analysis

The basic structure of the coupler to be discussed is as shown in Fig. 1. Variations on this geometry include cases with microstrip lines on the same side of the slot; multilayered substrates/superstrates; reverse couplers where the lines exit on the same wall; and with additional parallel slots and lines, among others, but can all be analyzed using the same approach.

The analysis proceeds as follows: the slot is replaced on both sides by an equivalent magnetic current backed by a perfectly conducting wall, representing the tangential electric field in the slot (all walls will be assumed to be perfect conductors). The problem is thereby separated into independent regions, coupled together by magnetic currents as shown in Fig. 2. This figure illustrates the treatment of finite slot thickness by introducing an intervening cavity. Eliminating the cavity and replacing $\overline{K}_L$ and $\overline{K}_U$ by $\overline{K}$ reduces the slot to the infinitesimally thin case which will be assumed here. Using the same current on either side enforces the continuity of the electric field in the slot. The fields in the cavities can now be written in term's of integrals as follows:

$$\overline{E} = -j\omega\mu \iint \overline{\overline{G}}_{eJ} \cdot \overline{J}\, dS' - \iint \overline{\overline{G}}_{eK} \cdot \overline{K}\, dS' \quad (1)$$

0018-9480/92$03.00 © 1992 IEEE

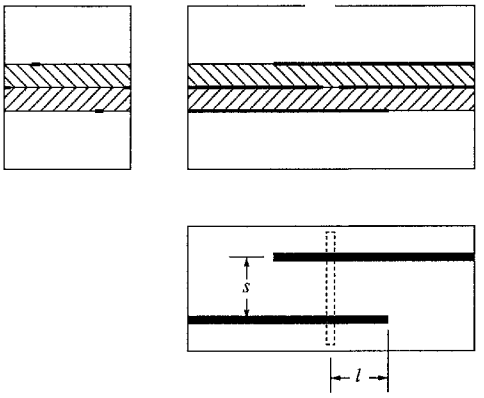

Fig. 1. Geometry of basic coupler.

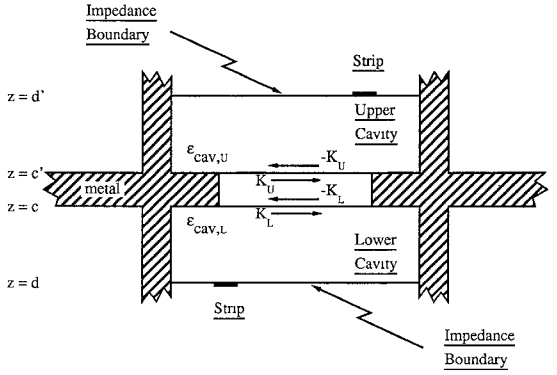

Fig. 2. Electric and equivalent magnetic currents for microstrip-to-microstrip coupler with a "thick" slot.

$$\bar{H} = \iint \bar{\bar{G}}_{mJ} \cdot \bar{J}\, dS' - j\omega\epsilon \iint \bar{\bar{G}}_{mK} \cdot \bar{K}\, dS' \qquad (2)$$

The subscripts on the Green's functions indicate whether the function is of the electric (e) or magnetic (m) field type for electric (J) or magnetic (K) currents.

By using the appropriate rectangular cavity Green's functions, the fields in the cavities satisfy the boundary conditions on the walls. The remaining boundary conditions, zero tangential electric fields on the strips and continuous tangential magnetic fields in the slot, allow us to write the integral equations which are

$$-j\omega\mu \iint_{\text{strip}L} \bar{\bar{G}}_{eJ} \cdot \bar{J}_L\, dS' - \iint_{\text{slot}} \bar{\bar{G}}_{eK} \cdot \bar{K}\, dS' = 0^* \qquad (3)$$

$$\iint_{\text{strip}L} \bar{\bar{G}}_{mJ} \cdot \bar{J}_L\, dS'$$

$$- j\omega \iint_{\text{slot}} [\epsilon_L \bar{\bar{G}}_{mK} + \epsilon_U \bar{\bar{G}}_{mK}] \cdot \bar{K}\, dS'$$

$$- \iint_{\text{strip}U} \bar{\bar{G}}_{mJ} \cdot \bar{J}_U\, dS' = 0 \qquad (4)$$

$$\iint_{\text{slot}} \bar{\bar{G}}_{eK} \cdot \bar{K}\, dS' - j\omega\mu \iint_{\text{strip}U} \bar{\bar{G}}_{eJ} \cdot \bar{J}_U\, dS' = 0^* \qquad (5)$$

where 0* implies that the field is nonzero at gap generator locations. Equations (3) and (5) are evaluated on the lower and upper strips respectively, and (4) on the slot. The subscripts U and L indicate whether the source is in the upper or lower cavity.

The longitudinal current components are now expanded in terms of piecewise sinusoidal functions with a Maxwellian transverse distribution satisfying the edge conditions for narrow strips and slots. In general, the currents are written in terms of both longitudinal and transverse components however, in this case, it will be assumed that both the slot and the strips are narrow enough so that the longitudinal components of current dominate their behavior and the transverse components can be neglected. The integral equations can now be written as a generalized matrix equation in conventional method of moments fashion. Using Galerkin's procedure, the matrix is nearly symmetric, the exception being the negative signs in the off-diagonal quadrants representing the coupling terms between the slot and microstrip lines:

$$\begin{bmatrix} \boldsymbol{Z}_{LL} & \boldsymbol{Y}_{LK} = -\boldsymbol{Z}_{KL}^T & 0 \\ \boldsymbol{Z}_{KL} = -\boldsymbol{Y}_{LK}^T & \boldsymbol{Y}_{LL} + \boldsymbol{Y}_{UU} & \boldsymbol{Z}_{KU} = -\boldsymbol{Y}_{UK}^T \\ 0 & \boldsymbol{Y}_{UK} = -\boldsymbol{Z}_{KU}^T & \boldsymbol{Z}_{UU} \end{bmatrix}$$

$$\begin{bmatrix} \boldsymbol{I}_L \\ \boldsymbol{V}_K \\ \boldsymbol{I}_U \end{bmatrix} = \begin{bmatrix} \boldsymbol{0}^* \\ \boldsymbol{0} \\ \boldsymbol{0}^* \end{bmatrix} \qquad (6)$$

where T indicates a transposed matrix and the "*" indicates the exceptions at the gap generators used for excitation of the lines. In addition to the relations indicated, for a symmetric structure only three of the submatrices are unique and the matrix will then have "mirror" symmetry with respect to the cross diagonal when properly loaded. The structures discussed here will be assumed lossless and symmetric for simplicity, although the more general case can be handled with the same approach.

The inverted matrix is then used with even and odd gap generator excitations at the line ends to find the currents on the microstrip lines. From the even and odd currents, even and odd impedances are found by measuring d defined as the relative distance from a standing wave maxima to the location of the slot. The expression for the reflection coefficient referenced to the slot then reduces to

$$\Gamma = -e^{j4\pi d/\lambda_g} \qquad (7)$$

which produces an impedance according to

$$Z = \frac{1 + \Gamma}{1 - \Gamma}. \qquad (8)$$

The even and odd impedances are then combined to form the Z-parameters which, because of the assumed sym-

metry are given by the simple expressions:

$$Z_{11} = \frac{Z_o + Z_e}{2} = Z_{22} \tag{9}$$

$$Z_{21} = \frac{Z_o - Z_e}{2} = Z_{12}. \tag{10}$$

Finally, the even and odd impedances may be combined to produce S-parameters through the transformations:

$$S_{11} = \frac{Z_{11}^2 - Z_{21}^2 - 1}{Z_{11}^2 + 2Z_{11} - Z_{21}^2 + 1} = S_{22} \tag{11}$$

$$S_{21} = \frac{2Z_{21}}{Z_{11}^2 + 2Z_{11} - Z_{21}^2 + 1} = S_{12} \tag{12}$$

which are used to characterize the coupling behavior.

III. Derivation of the Dyadic Green's Functions

In order to solve the integral equations, the Dyadic Green's functions must be known. They are solutions to the dyadic Helmholtz equations:

$$\nabla \times \nabla \times \overline{\overline{G}}_{eJ} - k^2 \overline{\overline{G}}_{eJ} = \bar{\bar{I}}\delta(\bar{R} - \bar{R}') \tag{13}$$

$$\nabla \times \nabla \times \overline{\overline{G}}_{mJ} - k^2 \overline{\overline{G}}_{mJ} = \nabla \times [\bar{\bar{I}}\delta(\bar{R} - \bar{R}')] \tag{14}$$

$$\nabla \times \nabla \times \overline{\overline{G}}_{mK} - k^2 \overline{\overline{G}}_{mK} = \bar{\bar{I}}\delta(\bar{R} - \bar{R}')] \tag{15}$$

$$\nabla \times \nabla \times \overline{\overline{G}}_{eK} - k^2 \overline{\overline{G}}_{eK} = \nabla \times \bar{\bar{I}}\delta(\bar{R} - \bar{R}') \tag{16}$$

where the primed vectors throughout, in this case $\bar{R}'$, indicate a function of the source coordinates. As can be seen, these equations are highly symmetric and in fact, once we have solved one set, the solution to the second set is almost trivial. Note however, that while the second pair of equations can be produced by application of the Duality Principle, the solutions cannot because duality does not apply to the boundary conditions [13]. The equations may be solved by a variety of techniques including vector potential methods or, as we have done, through a field expansion method which represents the solutions in terms of vector wave functions (VWF's). This latter approach has been developed to a straightforward procedure employing dyadic analysis to produce all components of the dyads in one exercise. For the sake of brevity, only the final results with be given here. A more detailed derivation is available in [14].

The Green's functions can be generalized to represent any layered structure of the type illustrated in Fig. 3. The use of impedance boundary conditions allow for the treatment of multi-layered substrates and superstrates as may be encountered in monolithic or other microwave circuits. The procedure is to find the Green's function for the layer containing the strip or slot by applying transmission line theory to the other layers to obtain the impedance boundary conditions (η) corresponding to each mode. Subsequently, the fields in the other layers can be found from the homogeneous solutions to (13)–(16) and a pair of coupling coefficients for each layer. The solutions are expanded in terms of LSE and LSM modes to facilitate finding the fields in the remaining layers since these modes are decoupled on the boundaries and can be individually matched to identical modes in adjacent layers. This also produces a one-to-one uniqueness in the impedance condition for each mode. The coupling coefficients are then readily found by matching the tangential field components at successive layers.

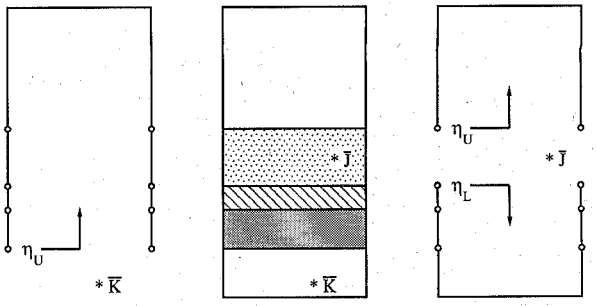

Fig. 3. Impedance boundary condition representation of a sample multilayered structure.

The impedance boundary conditions require the fields to satisfy

$$\eta = \frac{\hat{x} \cdot \bar{E}}{\hat{y} \cdot \bar{H}} : \frac{\hat{x} \cdot \nabla \times \overline{\overline{G}}_{mJ}}{\hat{y} \cdot \overline{\overline{G}}_{mJ}} = j\omega\epsilon\eta. \tag{17}$$

For simpler notation, η_e will be the wave impedance associated with the LSE modes and η_m will be used for the LSM modes. $\tilde{\eta}_e$ and $\tilde{\eta}_m$ will denote normalization to the wave impedances in each layer and are defined as

$$\tilde{\eta}_{ei} = \frac{k_{zi}\eta_{ei}}{\omega\mu} \quad \tilde{\eta}_{mi} = \frac{\omega\epsilon\eta_{mi}}{k_{zi}}. \tag{18}$$

These impedance boundary conditions derive from the recognition that the layered structures are simply sequential sections of homogeneously filled rectangular waveguide sections. We can then evaluate the impedance conditions using transmission line analysis and the wave impedances for the various layers as illustrated in Fig. 3. The impedances on a given layer upper boundary are found by the transmission line equation

$$\tilde{\eta}_{ei} = \frac{k_{zi}}{k_{z(i-1)}} \left[\frac{\tilde{\eta}_{e(i-1)} + j \tan k_{z(i-1)} l_{(i-1)}}{1 + j\tilde{\eta}_{e(i-1)} \tan k_{z(i-1)} l_{(i-1)}} \right] \tag{19}$$

$$\tilde{\eta}_{mi} = \frac{\epsilon_i k_{z(i-1)}}{\epsilon_{(i-1)} k_{zi}} \left[\frac{\tilde{\eta}_{m(i-1)} + j \tan k_{z(i-1)} l_{(i-1)}}{1 + j\tilde{\eta}_{m(i-1)} \tan k_{z(i-1)} l_{(i-1)}} \right] \tag{20}$$

where the index i is iterated from the top wall ($\eta_{e0} = \eta_{m0} = 0$) through successive lower layers to the layer of interest (l_i is the thickness of the ith layer). A similar process is used for the lower layers in which case the iteration proceeds from the lowest layer upwards and the wave impedance is negative.

The final results can be written as

$$\overline{\overline{G}}_{mJ} = \sum_{m=0}^{\infty}\sum_{n=0}^{\infty} \frac{2j(2-\delta_{mn})k_i}{abk_z(k_x^2+k_y^2)} \left\{ \frac{\begin{pmatrix} \overline{\mathfrak{M}}_{oo}[\tilde{\eta}_{mU};\, k_x,\, k_y,\, k_z(z-c)]\ \overline{\mathfrak{N}}'_{oo}[\tilde{\eta}_{mL};\, k_x,\, k_y,\, k_z(z'-d)] \\ \overline{\mathfrak{M}}_{oo}[\tilde{\eta}_{mL};\, k_x,\, k_y,\, k_z(z-d)]\ \overline{\mathfrak{N}}'_{oo}[\tilde{\eta}_{mU};\, k_x,\, k_y,\, k_z(z'-c)] \end{pmatrix}}{(\tilde{\eta}_{mU}-\tilde{\eta}_{mL})\cos k_z(c-d) - j(\tilde{\eta}_{mU}\tilde{\eta}_{mL}-1)\sin k_z(c-d)} \right.$$

$$\left. + \frac{\begin{pmatrix} \overline{\mathfrak{N}}_{ee}[\tilde{\eta}_{eU};\, k_x,\, k_y,\, k_z(z-c)]\ \overline{\mathfrak{M}}'_{ee}[\tilde{\eta}_{eL};\, k_x,\, k_y,\, k_z(z'-d)] \\ \overline{\mathfrak{N}}_{ee}[\tilde{\eta}_{eL};\, k_x,\, k_y,\, k_z(z-d)]\ \overline{\mathfrak{M}}'_{ee}[\tilde{\eta}_{eU};\, k_x,\, k_y,\, k_z(z'-c)] \end{pmatrix}}{(\tilde{\eta}_{eU}-\tilde{\eta}_{eL})\cos k_z(c-d) - j(\tilde{\eta}_{eU}\tilde{\eta}_{eL}-1)\sin k_z(c-d)} \right\} \quad \text{for } z \gtrless z' \tag{21}$$

and

$$\overline{\overline{G}}_{eJ} = \frac{1}{k_i^2}\hat{z}\hat{z}\delta(\overline{R}-\overline{R}') + \sum_{m=0}^{\infty}\sum_{n=0}^{\infty} \frac{2j(2-\delta_{mn})}{abk_z(k_x^2+k_y^2)}$$

$$\cdot \left\{ \frac{\begin{pmatrix} \overline{\mathfrak{M}}_{ee}[\tilde{\eta}_{eU};\, k_x,\, k_y,\, k_z(z-c)]\ \overline{\mathfrak{M}}'_{ee}[\tilde{\eta}_{eL};\, k_x,\, k_y,\, k_z(z'-d)] \\ \overline{\mathfrak{M}}_{ee}[\tilde{\eta}_{eL};\, k_x,\, k_y,\, k_z(z-d)]\ \overline{\mathfrak{M}}'_{ee}[\tilde{\eta}_{eU};\, k_x,\, k_y,\, k_z(z'-c)] \end{pmatrix}}{(\tilde{\eta}_{eU}-\tilde{\eta}_{eL})\cos k_z(c-d) - j(\tilde{\eta}_{eU}\tilde{\eta}_{eL}-1)\sin k_z(c-d)} \right.$$

$$\left. + \frac{\begin{pmatrix} \overline{\mathfrak{N}}_{oo}[\tilde{\eta}_{mU};\, k_x,\, k_y,\, k_z(z-c)]\ \overline{\mathfrak{N}}'_{oo}[\tilde{\eta}_{mL};\, k_x,\, k_y,\, k_z(z'-d)] \\ \overline{\mathfrak{N}}_{oo}[\tilde{\eta}_{mL};\, k_x,\, k_y,\, k_z(z-d)]\ \overline{\mathfrak{N}}'_{oo}[\tilde{\eta}_{mU};\, k_x,\, k_y,\, k_z(z'-c)] \end{pmatrix}}{(\tilde{\eta}_{mU}-\tilde{\eta}_{mL})\cos k_z(c-d) - j(\tilde{\eta}_{mU}\tilde{\eta}_{mL}-1)\sin k_z(c-d)} \right\} \quad \text{for } z \gtrless z' \tag{22}$$

where c and d are the upper and lower coordinates of the source layer. The δ_{mn} terms is the Kronecker delta defined as $\delta_{mn} = 1$ for $m = 0$ or $n = 0$ and zero otherwise. As indicated, the top lines apply for $z > z'$ and the bottom lines for $z < z'$ where primes throughout indicate functions of the source coordinates. The functions $\overline{\mathfrak{M}}$ and $\overline{\mathfrak{N}}$ are defined by

$$\overline{\mathfrak{M}}_{oo}[\eta,\, \alpha] = \eta\overline{M}_{ooo}[\alpha] + j\overline{M}_{ooe}[\alpha] \tag{23}$$

$$\overline{\mathfrak{M}}_{ee}[\eta,\, \alpha] = \eta\overline{M}_{eee}[\alpha] - j\overline{M}_{eeo}[\alpha] \tag{24}$$

$$\overline{\mathfrak{N}}_{oo}[\eta,\, \alpha] = \eta\overline{N}_{ooo}[\alpha] + j\overline{N}_{ooe}[\alpha] \tag{25}$$

$$\overline{\mathfrak{N}}_{ee}[\eta,\, \alpha] = \eta\overline{N}_{eee}[\alpha] - j\overline{N}_{eeo}[\alpha]. \tag{26}$$

The vector wave functions $\overline{M}$ and $\overline{N}$ are defined by

$$\overline{M} = \nabla \times \Psi\hat{x}_i = \frac{1}{k}\nabla \times \overline{N} \tag{27}$$

$$\overline{N} = \frac{1}{k}\nabla \times \nabla \times \Psi\hat{x}_i = \frac{1}{k}\nabla \times \overline{M} \tag{28}$$

where $k^2 = k_x^2 + k_y^2 + k_z^2$, Ψ is a scalar function and $\hat{x}_i$ is a unit vector called the "piloting vector" which determines the nature of the field expansion. In our case, choosing $\hat{x}_i = \hat{z}$, the normal to the layer interfaces, results in a correspondence between the leading $\overline{M}$ and $\overline{N}$ VWF's appearing in $\overline{\overline{G}}_{mJ}$ and the LSM and LSE modes, respectively. (In contrast, it should be noted that leading $\overline{M}$ and $\overline{N}$ functions correspond to the LSE and LSM modes, respectively, when they appear in $\overline{\overline{G}}_{eJ}$). The forms of Ψ are chosen to satisfy the boundary conditions on the walls of the cavity and are given by

$$\Psi_{\substack{ooo \\ eee}} = \begin{cases} \sin k_x x \sin k_y y \sin k_z z \\ \cos k_x x \cos k_y y \cos k_z z \end{cases} \tag{29}$$

$$\Psi_{\substack{ooe \\ eeo}} = \begin{cases} \sin k_x x \sin k_y y \cos k_z z \\ \cos k_x x \cos k_y y \sin k_z z \end{cases} \tag{30}$$

with $k_x = m\pi/a$, $k_y = n\pi/b$ and $k_z = \sqrt{k_i^2 - k_m^2 - k_n^2}$. The subscripts here and on the $\overline{M}$ and $\overline{N}$ functions indicate whether the trigonometric dependencies are even or odd (cosine or sine, respectively).

The solutions for the equivalent magnetic current $\overline{K}$ are virtually identical with the following notational replacements:

$$\overline{M} \Leftrightarrow \overline{N} \tag{31}$$

$$\overline{\overline{G}}_{eJ} \Rightarrow \overline{\overline{G}}_{mK} \tag{32}$$

$$\overline{\overline{G}}_{mJ} \Rightarrow \overline{\overline{G}}_{eK}. \tag{33}$$

Note that the $\overline{M} \Leftrightarrow \overline{N}$ replacements are what make these substitutions different from those dictated by the Duality Principle. It is these substitutions which compensate for the change in boundary conditions from the Dirichlet to Neumann conditions when the Duality Principle is applied. Expansion of these functions then yield all the components of the various Green's functions.

IV. Numerical and Experimental Results

A coupler with the geometry of Fig. 1 was analyzed using the above techniques. The parameters which can be varied in this design are numerous, consequently, only a few variations will be presented here. In all cases, although not required in general, symmetric geometry is maintained to simplify the even and odd mode analysis, as discussed above. Also, in all cases the cross-section for the cavity is 0.25 × 0.25 in.; the substrate is 0.025 in. thick with $\epsilon_r = 10.6$; and the slot and line widths are 0.025 in. The cavity length is varied for the numerical results and fixed at 2.0 in. for the measurements. This dimension does not affect the results since for all frequencies considered here, the cavity is below the cutoff frequency of the higher order microstrip modes and the reference plane was taken to be at the slot.

To illustrate the behavior of the coupler, we first examine the influence of various parameters at fixed operating frequencies. The effect of the line stub length (l) is shown in Fig. 4. It can be seen that the stub is initially too long for an ideal match at this frequency. However, as the stub is progressively shortened, a certain length "matches" the two port coupler and with further shortening the match gets progressively worse. We can interpret this effect by examining the equivalent circuit shown in Fig. 5. Variation of the stub length has the effect of changing the position of the current maxima (virtual shorts) and minima (virtual opens) on the lines relative to the slot, thus varying the degree of coupling through the slot represented by the coupling transformers. Consequently, the peak coupling occurs when line stub length places a current maximum below the slot or lengths in odd multiples of $\sim\lambda/4$. The opposite effect occurs when the line stub is approximately in multiples of $\lambda/2$ in length so that there is a virtual open circuit beneath the slot, in which case there would be very little coupling between the line and slot.

A similar effect is observed for variations in slot length (L_s) as illustrated in Fig. 6. Again using the transmission line analogy, one can interpret this effect by transforming the impedances at the ends of the slot to the center. These end impedances are nearly short circuits, the difference being due to fringing fields which extend beyond the ends of the slot line, fully accounted for by the full-wave analysis. At the matching length, the resulting transformed reactances at the center cancel the reactance associated with the junction, thereby matching the two ports. As the slot becomes very short, the field in the slot is effectively "short circuited," thus coupling is reduced. S_{21} then tends to zero while S_{11} approaches unity (since the structure is closed and assumed lossless). All of these effects would be expected to repeat as the slot length increases in multiples of λ, however, for the case studied here, the maximum slot length is limited by the dimensions of the shielding package which have been chosen to allow only the dominant microstrip mode to propagate.

To generate a frequency response, the programs are run at each frequency of interest and the slot and line lengths

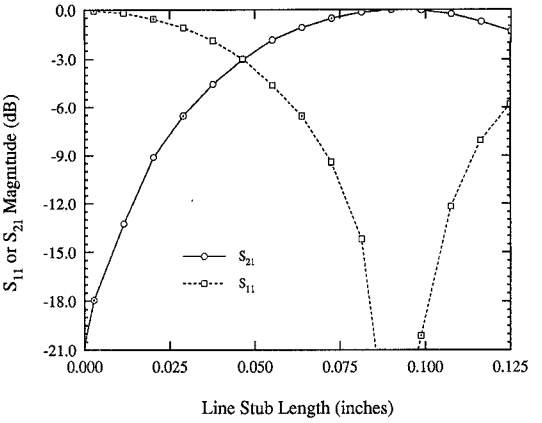

Fig. 4. Effect of the line stub length (l) on S_{21} and S_{11} magnitudes ($s = 0$, $L_s = 0.25$ inches and $f = 12.0$ GHz).

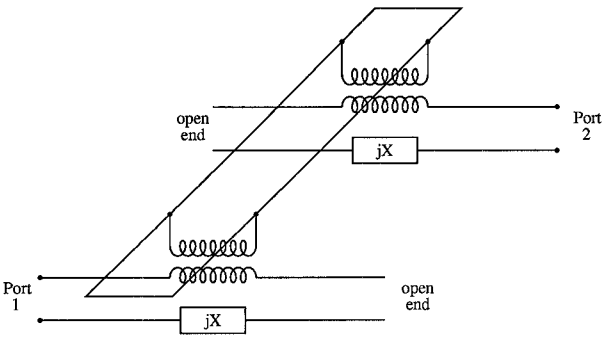

Fig. 5. Equivalent circuit for a 2-port coupler.

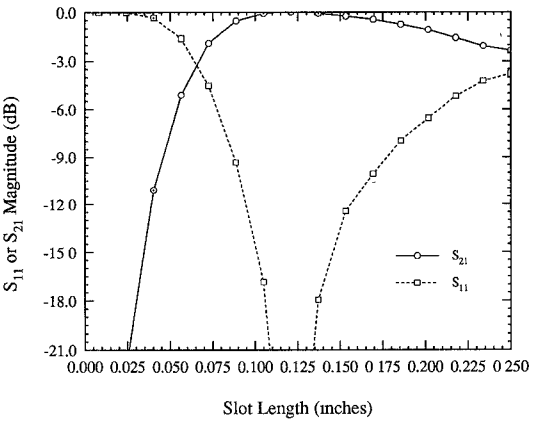

Fig. 6. Effect of the slot length on S_{21} and S_{11} magnitudes ($s = 0$, $l = 0.049$ inches and $f = 18.0$ GHz).

are varied to form a parametric database. (The most significant computation time is in the generation of the matrix. This takes approximately 30–45 min per frequency on an ~25 MIPS machine such as the IBM RS6000/320. One matrix is sufficient for all variations of slot and line stub lengths). The database is then scanned to assemble frequency response plots as a function of the geometric parameters. To verify the results, we have designed and constructed the fixture shown in Fig. 7. This fixture allows sample substrates with various line and slot dimensions to be installed in various combinations to allow fre-

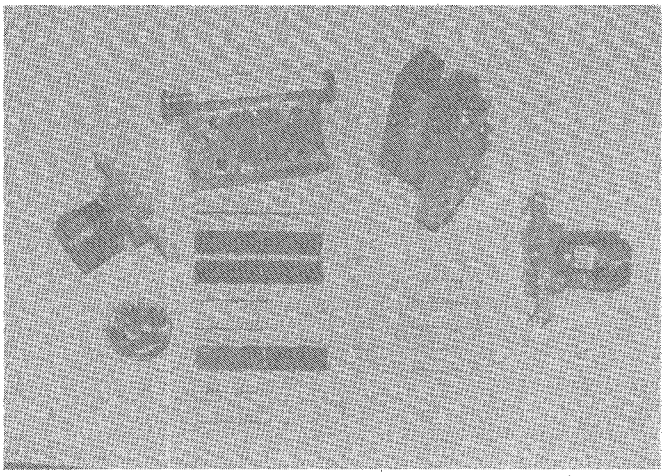

Fig. 7. Photograph of coupler fixture assembly.

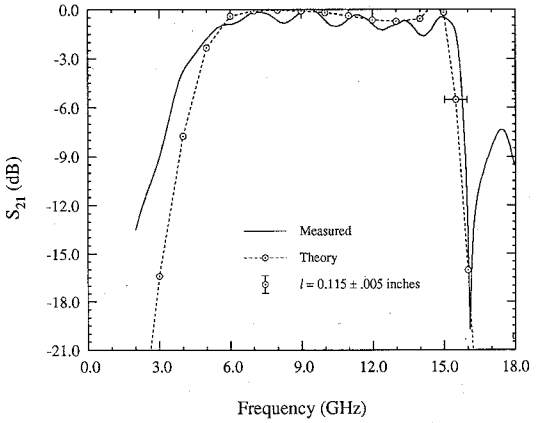

Fig. 8. Comparison of theory and experiment for S_{21} magnitudes with $s = 0$, $l = 0.115$ in., $L_s = 0.250$ in. The error bar indicates the influence on the high frequency corner by a ± 0.005 inch change in stub length.

quency response measurements. A number of circuit boards were made in two sets: One set of boards was double-sided with a microstrip line etched to certain lengths relative to a slot etched in the ground plane on the opposite side. The second set was one-sided boards with microstrip lines of corresponding lengths designed to be held against the boards of the first set by the fixture.

Measurement of one of the assemblies is shown in Fig. 8 in comparison to corresponding numerical results. The position of the high frequency corner of the response was found to be very sensitive to the length of the line stub. As discussed above, this corner is controlled by the length at which the stub is approximately $\lambda/2$. Since the effective dielectric constant for the microstrip is approximately $\epsilon_{\text{eff}} = 7.8$ at 17.0 GHz, a null is predicted in the response in that neighborhood so there is good agreement with the results shown. A theoretical curve for $l = 0.115$ inches is also shown which gives an indication of the sensitivity to the stub length. The error bar on the high end indicates the sensitivity of the high frequency corner to a ± 5 mil error in line stub length which is well within the expected tolerance errors for positioning the stubs relative to the slot, so we conclude that the results are in excellent agreement. In fact, we were able to move the upper board slightly toward the slot to expand the stub length somewhat which did shift the high corner to a lower frequency as expected. However, this also created problems with the match at the Eisenhart microstrip launchers so these results are not shown.

The "sidelobe" which can be seen at the high frequency end, is also attributed to tolerance errors for the line stub lengths. A difference in lengths would produce multiple nulls in the response at the high end which would be expected to have a sidelobe inbetween. Because of the high sensitivity to line length, owing in part to the high dielectric constant, the amplitude and span of the sidelobe is a strong function of the relative line stub lengths, which can also be observed when the boards are slightly shifted as described above. The sidelobes does not appear in the theoretical result since a difference in stub lengths between the upper and lower lines introduces an asymmetry which has not been included in the current numerical model and contradicts some of the assumptions stated for the network analysis. A more general model is planned to include this capability as well.

The ripple in all the measurements can be shown to result from mismatch at the microstrip launchers. The measurements are particularly sensitive to this connection because of the high dielectric constant of the substrate. They occurred in varying degrees throughout our measurements and are also influenced by small air gaps between the connector assembly, fixture and substrates. The ripple could probably be removed by more sophisticated deembedding techniques however this requires additional fixtures. Nevertheless, the ripple shown in the results presented here in not substantial and does not significantly interfere with the fundamental behavior of the devices. Also, the broadening of the low frequency response is typical in the measurements. We were not able to identify a direct cause for this effect, however, we suspect that it may also be related to the fixture/connector interface since we have not de-embedded these transitions. We also postulated that some of the anomalies might be caused by the side-wall grooves in the fixture which hold the double-sided board in place. This possibility was eliminated however by installing movable side-wall shorts which are visible in Fig. 7.

The remaining discrepancy is perhaps a slight additional loss found in some of the measured results. To deembed the losses for the structure, a through line was measured and the remaining measurements were post-processed to compensate for conductor and dielectric losses on the microstrip lines. This process however does not correct for losses associated with the slot including both conductor and dielectric losses and additional losses on the cavity walls, plus losses due to the added line lengths. The remaining differences are thus attributed to these factors together with measurement errors and are judged to be within acceptable limits.

Measurements on a different line stub length are shown

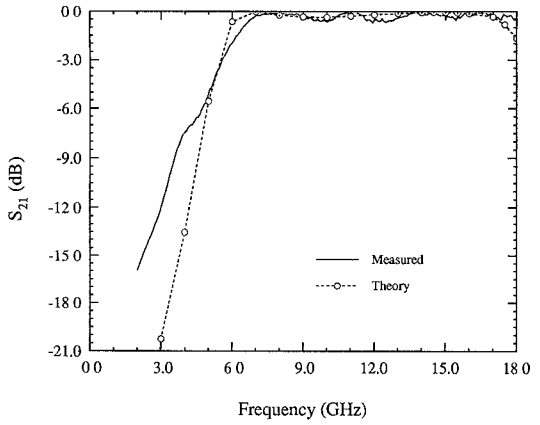

Fig. 9. Comparison of experiment and theory for S_{21} magnitudes with $s = 0$, $l = 0.080$ in., $L_s = 0.250$ in. illustrating the control of the high frequency corner with the line stub length by comparison with Fig. 8.

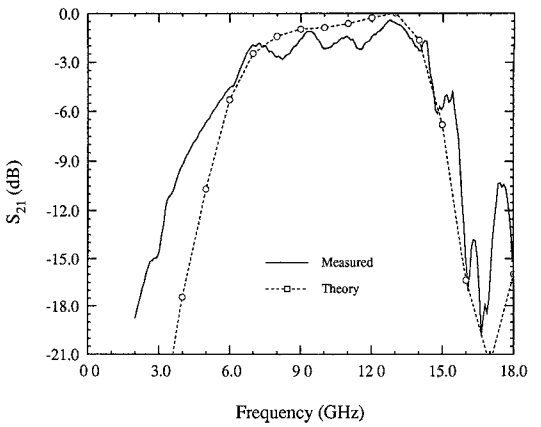

Fig. 11. Comparison showing the effect of line separation with $l = 0.115$ in., $L_s = 0.250$ in. and $s = 0.125$ in.

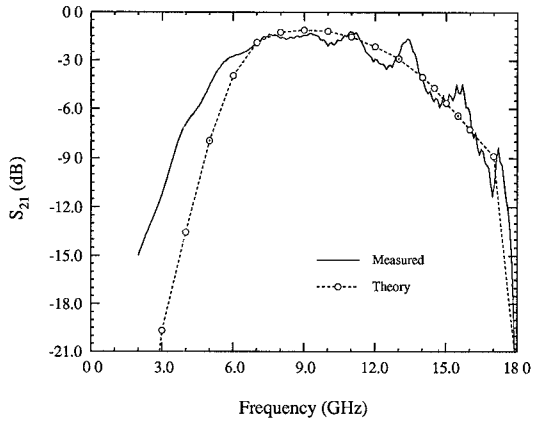

Fig. 10. Experimental and theory for S_{21} magnitudes with $s = 0$, $l = 0.110$ in., $L_s = 0.153$ in. showing the effect of shortening the slot length.

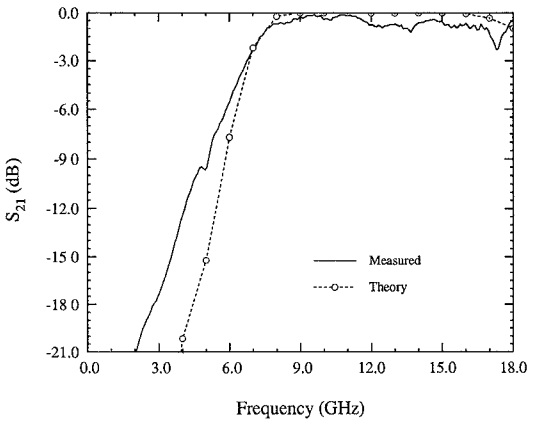

Fig. 12. The effect of line separation with shorter line stub length; $l = 0.080$ in., $L_s = 0.250$ in. and $s = 0.125$ in.

in Fig. 9 again showing good agreement with the theoretical results. In this case, the shortening of the stub length has moved the high frequency corner out of the range of the measurements. What is interesting to note about this case is that the low frequency corner of the response is quite insensitive to this change in stub length. Also of particular interest is the wide bandwidth of this transition.

Fig. 10 illustrates the effect of shortening the slot length. One consequence is reduced coupling in the passband which was also demonstrated in Fig. 6. We also see in this result, some movement of the high frequency null due to a shortening of the line stub length.

The final plots, Figs. 11 and 12, show the influence of the line separation parameter (s) on the frequency response. The figures correspond to Figs. 8 and 9, respectively, which have $s = 0$, showing in general, a narrowing of the frequency passband as s is increased. This is to be expected since we have now introduced an additional length parameter which can influence the response through its relationship to wavelength. Here again, the numerical model is judged to have correctly predicted the coupler behavior after the experimental artifacts are considered.

V. Conclusion

A set of integral equations for aperture coupled shielded microstrip lines has been introduced based on Green's function integrals and the Equivalence Principle. The associated dyadic Green's functions in the form of waveguide LSE and LSM modes have been derived which allow for a full-wave analysis, accounting for all electromagnetic interactions of the microstrip—slot coupler, including the capability for multi-layered substrates and superstrates. By expanding the unknown line currents and slot voltage in terms of subsectional basis functions and applying the method of moments together with even and odd mode transmission line analysis, the two-port scattering coefficients can be determined to characterize the coupling behavior.

The frequency response plots shown demonstrate the utility of the structure as an interconnect. With proper selection of the geometric parameters such as line and slot widths, lengths, line separation, substrate heights and materials, the frequency response can be tailored to give the required center frequency, bandwidth, shape, etc. As has been shown, very wide bandwidths can be achieved which makes the structure very versatile. Avoidance of via-holes

for RF transitions and their inherent limitations by the use of planar structures to form vertical interconnects, together with the ability of the model to accurately predict the coupler behavior as demonstrated by experimental results, are especially important considerations for design of monolithic circuits. In addition, although the approach discussed here uses certain simplifying assumptions about the symmetry of the structures, the technique can be readily adapted to the general case.

REFERENCES

[1] R. H. Jansen, R. G. Arnold, and I. G. Eddison, "A comprehensive CAD approach to the design of MMIC's up to MM-wave frequencies," *IEEE Trans. Microwave Theory Tech.*, vol. 36, no. 2, pp. 208–219, Feb. 1988.

[2] K. G. Gupta, R. Garg, and I. J. Bahl, *Microstrip Lines and Slotlines*. Norwood, MA: Artech House, 1979.

[3] T. Tanaka, K. Tsunoda, and M. Aikawa, "Slot-coupled directional couplers between double-sided substrate microstrip lines and their applications," *IEEE Trans. Microwave Theory Tech.*, vol. 36, no. 12, pp. 1752–1757, Dec. 1988.

[4] E. A. Mariani and J. P. Agrios, "Slot-line filters and couplers," *IEEE Trans. Microwave Theory Tech.*, vol. MTT-18, no. 12, pp. 1089–1095, Dec. 1970.

[5] M. Aikawa and H. Ogawa, "Double-sided MIC's and their applications," *IEEE Trans. Microwave Theory Tech.*, vol. 37, no. 2, pp. 406–413, Feb. 1989.

[6] S. B. Cohn, "Slot line on a dielectric substrate," *IEEE Trans. Microwave Theory Tech.*, vol. MTT-17, no. 10, pp. 768–778, Oct. 1969.

[7] E. A. Mariani, C. P. Heinzman, J. P. Agrios, and S. B. Cohn, "Slot line characteristics," *IEEE Trans. Microwave Theory Tech.*, vol. MTT-17, no. 12, pp. 1091–1096, Dec. 1969.

[8] J. B. Knorr, "Slot-line transitions," *IEEE Trans. Microwave Theory Tech.*, vol. MTT-22, no. 5, pp. 548–554, May 1974.

[9] H. Yang and N. G. Alexopoulos, "A dynamic model for microstrip-slotline transition and related structures," *IEEE Trans. Microwave Theory Tech.*, vol. 36, no. 2, pp. 286–293, Feb. 1988.

[10] S. Yamamoto, T. Azakami, and K. Itakura, "Slit-coupled strip transmission lines," *IEEE Trans. Microwave Theory Tech.*, vol. MTT-14, no. 11, pp. 542–553, Nov. 1966.

[11] B. Schüppert, "Microstrip/slotline transitions: Modeling and experimental investigatin," *IEEE Trans. Microwave Theory Tech.*, vol. 36, no. 8, pp. 1272–1282, Aug. 1988.

[12] H. Ogawa, T. Hirota, and M. Aikawa, "New MIC power dividers using coupled microstrip-slot lines: Two-sided MIC power dividers," *IEEE Trans. Microwave Theory Tech.*, vol. MTT-33, no. 11, pp. 1155–1164, Nov. 1985.

[13] R. E. Collin, *Field Theory of Guided Waves*. McGraw-Hill, 1960, pp. 29–34.

[14] N. L. VandenBerg, "Full-wave analysis of microstrip-fed slot antennas and couplers," Ph.D. dissertation, The University of Michigan, Ann Arbor, 1991.

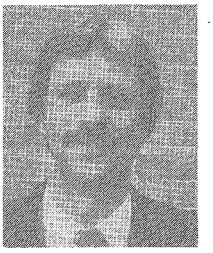

Norman L. VandenBerg (S'80–M'82–S'87–M'91) received the B.S.E.E., M.S.E.E., and Ph.D. degrees from the University of Michigan, Ann Arbor in 1980, 1982, and 1991, respectively.

From December 1982 to August 1987 he was employed by the Allied-Bendix Guidance Systems Division—Mishawaka Operations in Indiana, where he worked on experimental microwave and millimeter-wave spread spectrum radars. Since then he has worked at the Radiation Laboratory of the University of Michigan on numerical modeling of electromagnetic fields with applications to circuits and antennas.

Dr. VandenBerg is a member of Eta Kappa Nu, Tau Beta Pi and the IEEE AP, MTT and EMC societies.

Linda P. B. Katehi (S'81–M'84–SM'89) received the B.S.E.E. degree from the National Technical University of Athens, Greece, in 1977 and the M.S.E.E. and Ph.D. degrees from the University of California, Los Angeles, in 1981 and 1984 respectively.

In September 1984 she joined the faculty of the Electrical Engineering and Computer Science Department of the University of Michigan, Ann Arbor. Since then, she has been involved in the modeling and computer-aided design of millimeter-wave and near-millimeter-wave monolithic circuits and antennas.

In 1984 Dr. Katehi received the W. P. King Award and in 1985 the S. A. Schelkunoff Award from the Antennas and Propagation Society. In 1987 she received an NSF Presidential Young Investigator Award and an URSI Young Scientist Fellowship. She is a member of Sigma Xi.